



**HAL**  
open science

# An efficient method of 3-D elastic full waveform inversion using a finite-difference injection method for time-lapse imaging

Dmitry Borisov, Satish C Singh, Nobuaki Fuji

► **To cite this version:**

Dmitry Borisov, Satish C Singh, Nobuaki Fuji. An efficient method of 3-D elastic full waveform inversion using a finite-difference injection method for time-lapse imaging. *Geophysical Journal International*, 2015, 202, pp.1908 - 1922. 10.1093/gji/ggv268 . insu-01391633

**HAL Id: insu-01391633**

**<https://insu.hal.science/insu-01391633>**

Submitted on 3 Nov 2016

**HAL** is a multi-disciplinary open access archive for the deposit and dissemination of scientific research documents, whether they are published or not. The documents may come from teaching and research institutions in France or abroad, or from public or private research centers.

L'archive ouverte pluridisciplinaire **HAL**, est destinée au dépôt et à la diffusion de documents scientifiques de niveau recherche, publiés ou non, émanant des établissements d'enseignement et de recherche français ou étrangers, des laboratoires publics ou privés.

# An efficient method of 3-D elastic full waveform inversion using a finite-difference injection method for time-lapse imaging

Dmitry Borisov,<sup>1</sup> Satish C. Singh<sup>1</sup> and Nobuaki Fuji<sup>1,2</sup>

<sup>1</sup>Laboratoire de Géosciences Marines, Institut de Physique du Globe de Paris, Paris, France. E-mail: [dborisov@princeton.edu](mailto:dborisov@princeton.edu)

<sup>2</sup>Laboratoire de Sismologie, Institut de Physique du Globe de Paris, Paris, France

Accepted 2015 June 16. Received 2015 June 14; in original form 2014 September 26

## SUMMARY

Seismic full waveform inversion is an objective method to estimate elastic properties of the subsurface and is an important area of research, particularly in seismic exploration community. It is a data-fitting approach, where the difference between observed and synthetic data is minimized iteratively. Due to a very high computational cost, the practical implementation of waveform inversion has so far been restricted to a 2-D geometry with different levels of physics incorporated in it (e.g. elasticity/viscoelasticity) or to a 3-D geometry but using an acoustic approximation. However, the earth is three-dimensional, elastic and heterogeneous and therefore a full 3-D elastic inversion is required in order to obtain more accurate and valuable models of the subsurface. Despite the recent increase in computing power, the application of 3-D elastic full waveform inversion to real-scale problems remains quite challenging on the current computer architecture. Here, we present an efficient method to perform 3-D elastic full waveform inversion for time-lapse seismic data using a finite-difference injection method. In this method, the wavefield is computed in the whole model and is stored on a surface above a finite volume where the model is perturbed and localized inversion is performed. Comparison of the final results using the 3-D finite-difference injection method and conventional 3-D inversion performed within the whole volume shows that our new method provides significant reductions in computational time and memory requirements without any notable loss in accuracy. Our approach shows a big potential for efficient reservoir monitoring in real time-lapse experiments.

**Key words:** Inverse theory; Computational seismology; Wave propagation.

## 1 INTRODUCTION

Full waveform inversion (FWI) is now widely recognized as a powerful tool to extract information on subsurface structures from recorded seismic data (see Virieux & Operto 2009, for review). FWI is a data-fitting approach, minimizing the difference between observed and modelled data using an adjoint state technique (e.g. Tromp *et al.* 2005; Plessix 2006). The initial framework of FWI in the time–distance domain was proposed by Lailly (1983) and Tarantola (1984). Since FWI takes into account all information embedded in seismic data, including amplitudes and phases, models obtained using FWI have by definition a better resolution than those obtained using conventional approaches such as traveltimes tomography, dispersion curve analysis, etc. Moreover, since FWI is in general an automated methodology, for example, it does not require human eye-ball procedures such as traveltimes picking, it is very suitable for analysing a large amount of seismic data, particularly those acquired by seismic industry, but at a rather high computational cost. These advantages make the technique very attractive for seismic imaging and thus FWI has already found wide range of

applications in the geophysical community. For example, (i) FWI results are used as starting velocity models for seismic migration (e.g. Virieux & Operto 2009; Plessix *et al.* 2013). (ii) FWI is used in global seismology for imaging crustal, lithospheric and deep mantle structures (e.g. Ravaut *et al.* 2004; Operto *et al.* 2006; Arnulf *et al.* 2012). Recently, Kawai *et al.* (2014) and Konishi *et al.* (2014) inverted for localized deep mantle structures in detail using Hessian matrix and gradient calculated for 1-D Earth. Fichtner *et al.* (2009) are working on the upper mantle waveform tomography by calculating gradient and approximated Hessian. Lekić & Romanowicz (2011) and French *et al.* (2013) use asymptotic Hessian kernel, which is cheap to calculate, and reveal its capacity to image sharp structure in the whole mantle. (iii) FWI is also used at reservoir scale for monitoring (Gosselet & Singh 2007; Asnaashari *et al.* 2011, 2013, 2015; Zheng *et al.* 2011; Routh *et al.* 2012; Queißer & Singh 2013) and pore pressure estimation (Roberts *et al.* 2008).

Due to high computational cost, the implementation of FWI in the early 1980s was mainly restricted to the 2-D geometry using an acoustic approximation (Tarantola 1984) or using full elastic definition in the time–distance domain (Tarantola 1986; Mora 1987).

During that time, FWI was mainly applied to near offset reflection data. Although the early 2-D FWI results were encouraging, the industry opted for 3-D migration of seismic reflection data as a main tool for seismic imaging because of its quality of images and cost-effectiveness. Shipp & Singh (2002) included inversion of long offset reflection and refraction data and showed that it can provide accurate medium to short wavelength of velocity information. Pratt *et al.* (1996) showed that inverting a single discrete frequency from refraction data and increasing the frequency, one can retrieve medium wavelength velocity information very efficiently. The method was applied to wide-aperture data using acoustic approximation and has been recently extended to 3-D geometry (Ben-Hadj-Ali *et al.* 2008; Plessix 2009; Sirgue *et al.* 2010).

However, the acoustic approximation could lead to erroneous updates in the velocity model in the inversion (e.g. Plessix *et al.* 2013). This becomes particularly important in the presence of strong elastic contrasts where errors arise due to overfitting of the observed elastic data by acoustically modelled synthetics (e.g. Barnes & Charara 2009). Several studies succeeded in reconstructing 2-D elastic parameters independently, in particular,  $V_p$  and  $V_s$  for both marine (e.g. Sears *et al.* 2008) and land long offset (e.g. Brossier *et al.* 2009).

However, there are two problems in performing 2-D elastic FWI. The first problem is associated with 3-D scattering effect that cannot be handled correctly using 2-D FWI (e.g. Mufti 1989). The second problem is due to the 2-D approximation used for sources (line source) in computing synthetic data where the real sources are in 3-D (point source), leading to erroneous amplitude due geometrical spreading. Generally, a temporal scaling using  $\sqrt{t}$  could be applied to correct the amplitude, but it is not as accurate as expected (e.g. Wapenaar *et al.* 1992b), particularly for the inversion of  $S$ -wave velocity models.

In the reality, however, the Earth is three-dimensional, elastic and highly heterogeneous, and therefore, one would require a full 3-D elastic inversion for more accurate imaging. Recently, 3-D elastic FWI has been developed and tested on synthetic data sets (Borisov & Satish 2013; Butzer *et al.* 2013; Vigh *et al.* 2013) and applied to small-scale real data sets with shallow targets (Guasch *et al.* 2012; Vigh *et al.* 2014). Borisov & Singh (2015) have shown that both 2-D elastic and 3-D acoustic approximation provide poor inversion results as compared to 3-D elastic FWI. However, the application of 3-D FWI to realistic model dimensions remains challenging even with modern computational resources. One can reduce the computational cost by extrapolating or redatuming the surface data in depth performing 3-D FWI in a localized area, for example in the vicinity of a reservoir. Dong *et al.* (2009) used a ray-based Kirchhoff's method to efficiently redatum the data close to the target, and then performed one-way wave-equation migration. Yang *et al.* (2012) used a similar approach for redatuming and performed acoustic FWI to time-lapse seismic data. However, in order to perform the wavefield extrapolation, one needs to know accurately about the base-line model between the Earth's surface and the target region. We suggest that a 3-D elastic FWI should be applied first to whole low frequency data to get the base-line velocity model.

In this paper, we develop an efficient way to perform 3-D elastic waveform inversion of time-lapse seismic data using Finite-Difference Injection Method (FDIM; Robertsson & Chapman 2000). FDIM allows us to calculate synthetic seismograms efficiently after model alterations in a localized region. The method is based on the wavefield superposition and its representation integral along the boundary. It requires only one calculation for a full volume and then iterates calculations in the subvolume and its neighbour-

hood, allowing significant reductions in computational time and memory requirements. A similar approach was used by Monteiller *et al.* (2013) and Masson *et al.* (2013) to compute synthetic data in spherical earth model. Our inversion approach here is based on the 2-D FWI initially developed by Royle (2010) and Singh & Royle (2010).

## 2 FORWARD MODELLING

Throughout this study, we calculate synthetic seismograms using a 3-D staggered grid based on a fourth-order accuracy in space and second-order accuracy in time (e.g. Randall 1989; Graves 1996). Fig. 1 shows a schematic illustration of our staggered FD grid in a 2-D slice. Note that particle velocity, stress components and elastic parameters are stored at different locations, hence we are obliged to interpolate those values when we need to know different kinds of variables at a certain point. For this purpose we used a simple linear interpolation. One can apply more sophisticated techniques, such as approximation using the *sinc* function tapered with a Kaiser function (Hicks 2002), which might improve the accuracy but it is out of scope in this paper.

Consider a strong form of first-order partial differential equations, which describes the 3-D elastic wave propagation in a velocity–stress formulation in a 3-D Cartesian coordinate system:

$$\rho \frac{\partial v_i}{\partial t} = \tau_{ij,j} + f_i \quad (1a)$$

$$\rho \frac{\partial \tau_{ij}}{\partial t} = \frac{1}{2} C_{ijkl} \{v_{k,l} + v_{l,k}\}, \quad (1b)$$

where  $v_i$  is the  $i$ th component of particle velocity,  $\tau_{ij}$  a stress tensor,  $f_i$  source term,  $\rho$  density and  $C_{ijkl}$  elastic moduli. If we assume an isotropic medium, the fourth-order elastic tensor reduces to

$$C_{ijkl} = \lambda \delta_{ij} \delta_{kl} + \mu (\delta_{il} \delta_{jk} + \delta_{il} \delta_{jk}), \quad (2)$$

where  $\lambda$ ,  $\mu$  denote the Lamé elastic parameters, and  $\delta$  is a Kronecker's delta. Eqs (1a) and (b) can be re-written in the following form:

$$\rho \frac{\partial v_i}{\partial t} = \tau_{ij,j} + f_i \quad (3a)$$

$$\rho \frac{\partial \tau_{ij}}{\partial t} = \lambda v_{k,k} \delta_{ij} + \mu (v_{i,j} + v_{j,i}). \quad (3b)$$

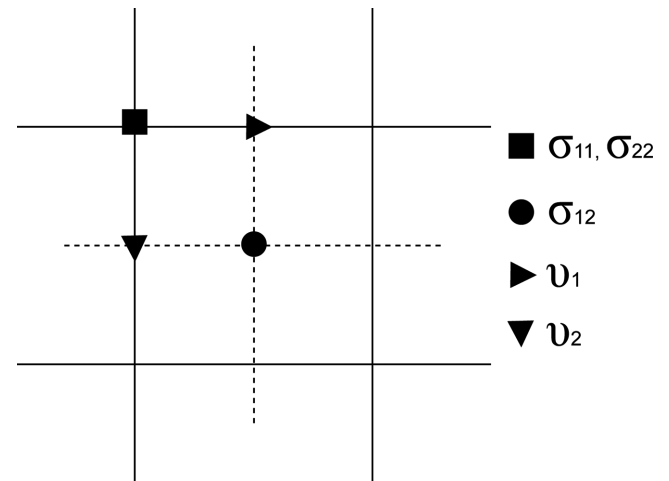


Figure 1. 2-D-FD staggered grid. Wavefield components and elastic parameters stored at different locations.

In this study, we restrict our calculations to isotropic elastic medium. However, the effects of attenuation and anisotropy can be included in a straightforward manner.

Since FWI spends most of its computational time on forward modelling, the successfulness of the inversion strongly depends on the balance between accuracy, efficiency and representation of physics included in the forward modelling solver. Our modelling algorithm is heavily parallelized using a domain decomposition technique on a distributed memory platform, allowing for an accurate and efficient wavefield computation for a 3-D geometry. Un-split convolutional perfectly matched layers (C-PMLs) are used to efficiently absorb undesirable reflections from the model boundaries (Komatitsch & Martin 2007).

We review briefly representation theorems for specific geometries before detailing our strategies for a localized waveform inversion since it is an important step to extrapolate the sources to the small region of calculation. Here we consider a reciprocity theorem for elastic equation of motion. First, in analogy to eq. (1), we define Green's functions in velocity–stress formulation with a source located at  $\mathbf{x}_B$ :

$$\rho \frac{\partial G_{il}^B}{\partial t} = \Sigma_{ijl,j}^B + g_i \quad (4a)$$

$$\rho \frac{\partial \Sigma_{ijl}^B}{\partial t} = \frac{1}{2} C_{ijkl} \{ G_{kl,m}^B + G_{ml,k}^B \} \quad (4b)$$

with

$$g_i = \delta(\mathbf{x} - \mathbf{x}_B) \delta(t - t_0) \delta_{il}, \quad (5)$$

where  $G_{il}^B = G_{il}(\mathbf{x}, \mathbf{x}_B)$  is the  $i$ th component of particle velocity and  $\Sigma_{ijl}^B = \Sigma_{ijl}(\mathbf{x}, \mathbf{x}_B)$  a stress tensor for a point source  $g_i$  at  $\mathbf{x}_B$  with an origin time  $t = t_0$ .  $\delta$  denotes either Kronecker's delta or Dirac's delta function. We arrange the sum of convolution of eq. (1a) and  $G_{il}^B$  and convolution of eq. (4a) with  $v_i$ , taking integral over an arbitrary volume  $V$  surrounded by surface  $S$ , we obtain a convolution-type representation theorem:

$$v_n(\mathbf{x}_B) = \int_V G_{in}^B * f_i dV + \int_S G_{in}^B * (\tau_{ij} n_j) dS - \int_S (\Sigma_{in}^B n_i) * v_i dS \quad (6)$$

where  $n_j$  is an outward normal to the surface  $S$ , as parentheses of the second and third terms in the right-hand side are tractions, and the star denotes convolution in time. Note that this representation theorem can be used for any arbitrary volume  $V$ .

When we have a source distribution  $f_i$  non-zero uniquely outside volume  $V$ , the first term on the right-hand side vanishes and we obtain:

$$v_n(\mathbf{x}_B) = \int_S [G_{in}^B * (\tau_{ij} n_j) - (\Sigma_{in}^B n_i) * v_i] dS. \quad (7)$$

We call the right-hand side 'representation integral' (e.g. Aki & Richards 2002). This representation theorem relates itself to convolution-type interferometry (e.g. Halliday & Curtis 2010). The key idea is that we can express seismic records by interfering wavefields due to the source distribution  $f_i$  and Green's functions from the receivers over a certain closed surface. However, in our localized inversion approach and in many other situations in exploration geophysics, it is not possible to place the receivers all around the closed surface. In these cases, we use a 'truncated version' of representation integral

$$v_i(\mathbf{x}_B) = \int_{S'} [G_{il}^B * (\tau_{ij} n_j) - (\Sigma_{ijl}^B n_j) * v_i] dS, \quad (8)$$

supposing that the quantity

$$\int_{S'} [G_{il}^B * (\tau_{ij} n_j) - (\Sigma_{ijl}^B n_j) * v_i] dS$$

vanishes, when we take  $S'$  infinitely far and deep. In this paper, we set the truncated surface  $S'$  horizontally below or on the surface of the Earth and reconstruct virtual sides of either source or receiver.

### 3 FINITE-DIFFERENCE INJECTION METHOD

The FDIM was originally proposed by Alterman & Karal (1968) for implementation of a point source in the FD method and was later on adopted by Robertsson & Chapman (2000) to perform efficient seismic modelling after a local model alteration. This approach is referred to as the full field/scattered method in the electromagnetism community (e.g. Taflove & Hagness 2005). Several studies proposed in computational seismology to use hybrid modelling for efficient calculation of synthetic seismograms. In hybrid methods the computational domain is divided into several domains in which wave propagation is computed separately, often with different methods (e.g. Capdeville *et al.* 2002, 2003; Bouchon & Sánchez-Sesma 2007; Godinho *et al.* 2009; Opršal *et al.* 2009; Monteiller *et al.* 2013). Masson *et al.* (2013) introduced general concept of time-reversal mirrors for regeneration of forward and backward propagations in an arbitrary localized region by finding local equivalent body forces.

Within the FDIM, the numerical simulations achieved by injecting the wavefield inside a subdomain in the manner described in the next subsection, without re-calculating the wavefield over the whole model space. The implementation is entirely based on the traditional FD schemes (e.g. Boore 1972; Madariaga 1976; Virieux 1986; Levander 1988).

In the next section we briefly recall the theory of the FDIM. Then, we demonstrate a synthetic time-lapse example, where FDIM was used to efficiently calculate the updated seismic records after local model perturbations within the 3-D elastic medium.

#### 3.1 Wavefield injection

The main idea of the FDIM is to satisfy the principles of superposition and continuity of the wavefield. Since the method depends on a connecting solution in different regions, the main computational domain is divided into several subvolumes. These subvolumes and their surrounding surfaces play a crucial role.

Fig. 2(a) schematically illustrates a conventional seismic survey, where the source and receivers placed close to the surface of the Earth, while the zone of interest is located at some depth. Fig. 2(b) illustrates new virtual locations of the source and receivers employed within the FDIM. The region where the physical properties are altered (e.g. producing oil/gas reservoir or a reservoir for CO<sub>2</sub> storage) is referred to injection subvolume  $V_i$ . The injection surface  $S_i$  encloses this altered region and essentially, this surface replaces the point source used in the conventional modelling. Alterman & Karal (1968) showed that it is possible to introduce a wavefield into a subvolume from a source located outside by injecting an analytical solution along a closed surface. Similarly, the wavefield recorded along the closed surface  $S_i$  can be used as a source to compute the wavefield within the interior region. Submesh  $V_e$  surrounding the subvolume  $V_i$  is used to limit the part of the initial model where the seismic wavefield will be recomputed. The associated

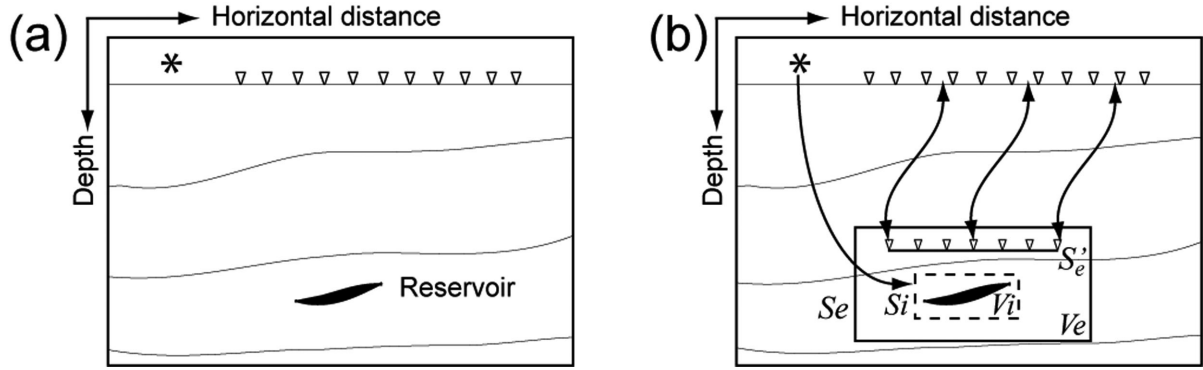


**Figure 2.** (a) Initial model with source and receivers placed at the surface. (b) New source and receivers position close to the reservoir.  $S_i$  and  $V_i$  are the injection surface and subvolume, respectively, encompassing the zone of interest.  $V_e$  is an FD submesh, which limits the area of the calculations and surface  $S_e$  acts as an absorbing boundary. The star indicates a source, the surface receivers are shown as the triangles. Adopted from Robertsson & Chapman (2000).

surface  $S_e$  simply acts as an absorbing boundary, which is regularly employed on the horizontal and lower edges of the model in order to prevent undesirable reflections from the artificial borders. As our localized inversion strategy requires seismic records to be within the subvolume  $V_e$ , we denote the location of virtual receivers by surface  $S'_e$ .

Suppose that the initial response to the unaltered model equals to  $\{v_i^I, \tau_{ij}^I\}$ . We can then recalculate the seismic wavefield  $\{v_i^R, \tau_{ij}^R\}$  inside the altered region  $V_i$  by injecting the wavefield  $\{v_i^I, \tau_{ij}^I\}$  along the surface  $S_i$ . The process of the wavefield injection for the velocity components is governed by the following updates:

$$v_i(\mathbf{x}) = v_i^R(\mathbf{x}) \quad \text{for } \mathbf{x} \in V_i \quad (9a)$$

$$v_i(\mathbf{x}) = v_i^R(\mathbf{x}) + v_i^I(\mathbf{x}) \quad \text{for } \mathbf{x} \in V_e \cap \bar{V}_i \quad (9b)$$

$$v_i(\mathbf{x}) = v_i^I(\mathbf{x}) + \int_{S'_e} (G_{ik}(\mathbf{x}', \mathbf{x}) * \tau_{kj}^R(\mathbf{x}') - \Sigma_{ijk}(\mathbf{x}', \mathbf{x}) * v_k^R(\mathbf{x}')) n_j dS' \quad \text{for } \mathbf{x} \in \bar{V}_e. \quad (9c)$$

The updates for the stress components (or pressure) can be described in the same way. The integral in eq. (9c) corresponds to a truncated version of the representation integral as in eq. (7), that is,  $S'_e$  should be in fact a closed surface but there is little interaction through the other masked surfaces and thus we can ignore them. The Green's functions are calculated in the initial unaltered model, by inducing impulsive point sources from the receivers located on the Earth surface to the point of integration located at the level  $S'_e$ . In practice, band-limited Green's functions between two points can be used to solve eqs (9) if an accurate estimation of the model is available (Wapenaar *et al.* 1992a; Dong 2008). Therefore, eq. (9c) is used to extrapolate to the surface the wavefield that was recorded at the datum located in the proximity of the target area. For localized approach, before applying inversion one would prefer to extrapolate initially observed wavefield from the surface receivers to some level closely located to the zone of interest using the same eq. (9c).

From eqs (9b) and (c) one can conclude that FDIM requires the initial wavefield  $\{v_i^I, \tau_{ij}^I\}$  to be calculated in the entire grid using eq. (3) first. At each time step of the full FD simulation, the wavefield is recorded along the injection surface  $S_i$ . For the fourth-order accurate FD scheme, we need values of  $v_i^I$  and  $\tau_{ij}^I$  stored in the external file at three grid points around the surface  $S_i$ . The following FD simulations are restricted to the subvolume  $V_e$

only. During these local simulations, at each time step the recorded wavefield is injected into the staggered grid in the manner illustrated in Fig. 3 for tractions where two different situations are shown. If the update is performed for the components located inside  $V_i$  (Fig. 3, left), the wavefield is supposed to propagate in the whole medium. Velocity fields are thus added at the positions where the parts of the fourth-order stencil go outside the  $V_i$  (eq. 9b). If the update is performed for the components located outside  $V_i$  (Fig. 3, right), it is assumed that there is no wavefield injection. Therefore, the velocity fields subtracted at the positions where the parts of the fourth-order stencil situated inside the subvolume  $V_i$  (eq. 9a).

The wavefield recalculated in such a manner can provide accurate seismic response after local model alterations (Robertsson & Chapman 2000). The amplitude of the variations can be arbitrarily large. The only missing part in the recalculated seismograms is the so-called long-range interactions, resulting from the altered wavefield interaction with the unaltered model outside the FD-submesh  $S_e$ , which propagates back. However, wavefield generated by such interactions would arrive after the primary altered wavefield, and would have a limited effect on localized FWI. If the model just above the submesh has a strong velocity contrasts, then this part of the model should be included in the submesh in order to avoid adverse effect. One can also use an exact boundary condition to address the issue of high-order long-range interactions (van Manen *et al.* 2007), but in this study we do not follow such an extension due to the increased complexity in the implementation and the significant additional computing efforts associated with the calculation of a larger number of the Green's functions, particularly for inversion.

### 3.2 Example of forward modelling using the FDIM

Here we illustrate a synthetic example, where the FDIM is used for an efficient re-calculation of the seismograms, after local model perturbations. For this purpose we use a horizontally layered model (Fig. 4a), where  $P$ - and  $S$ -wave velocities are linked to each other through a simple arithmetic factor of 1.5. The density parameter is derived from the  $P$ -wave velocity using the empirical relationships of Gardner *et al.* (1974) and Hamilton (1978). The minimal value of  $S$ -wave velocity below the water layer is equal to  $1200 \text{ m s}^{-1}$ . Although such high  $S$ -wave velocity corresponds to a high-contrast seafloor, which is relatively rare, we use this high  $S$ -wave velocity in this numerical experiment in order to discretize the medium sparsely.

The model contains a volume of  $8 \times 4 \times 8 \text{ km}$  in inline ( $x$ ), depth ( $z$ ) and crossline ( $y$ ) directions, respectively. We discretize

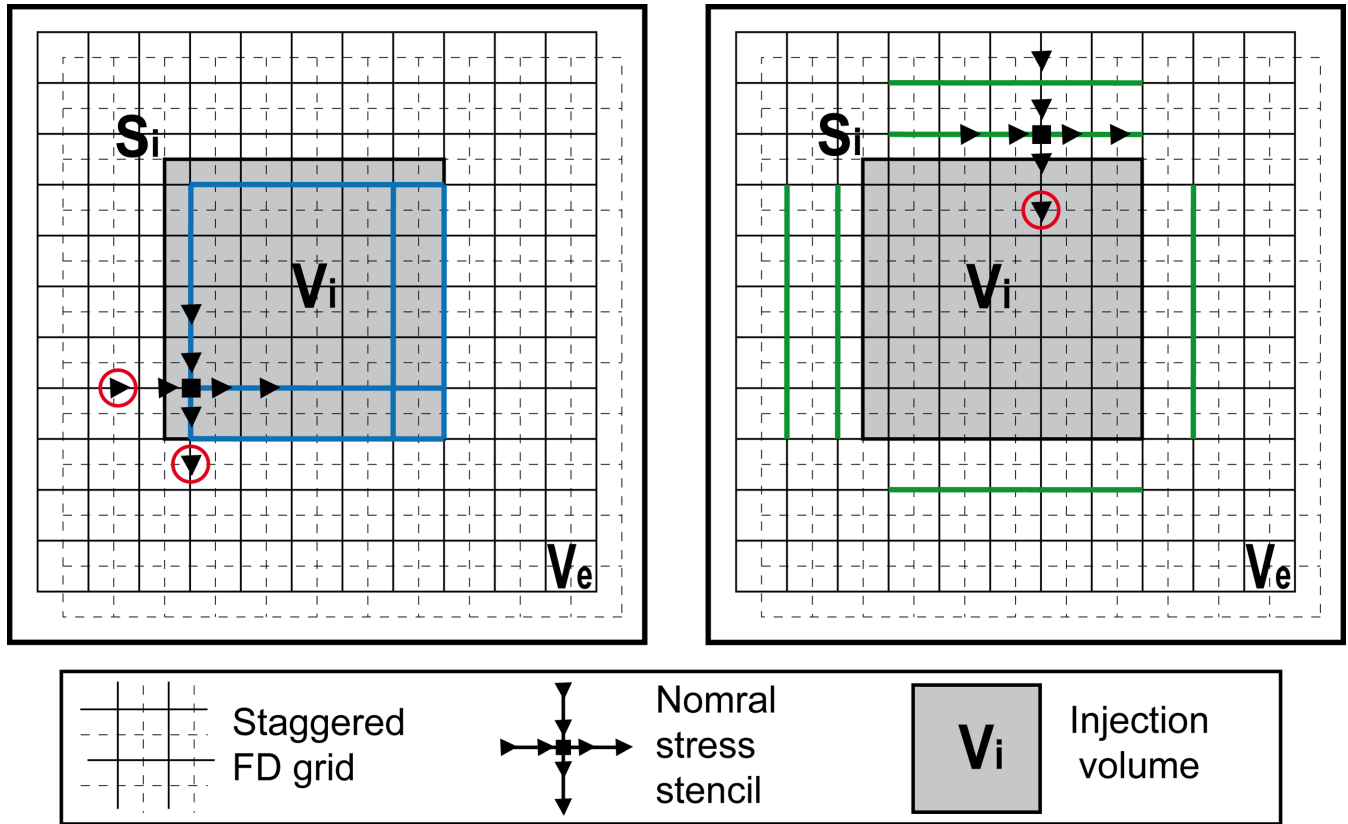


**Figure 3.** The process of wavefield injection in the 2-D staggered FD grid (adopted from Robertsson & Chapman 2000). Update for the normal component of stress is illustrated within fourth-order accurate FD scheme (stencil is shown on both pictures with notation specified in Fig. 1). Left: when the stress is updated inside  $V_i$ , the velocity component recorded during the full FD simulation should be added at the position indicated by red circles, where the stencil intersects the surface  $S_i$  (eq. 9b). Right: when the stress is updated outside  $V_i$ , the velocity component recorded during the full FD simulation should be subtracted at the position indicated by red circles, where the stencil intersects the surface  $S_i$  (eq. 9a). Blue and green lines indicate the location of the stress components where the addition and subtraction of particle velocity components are required, respectively.

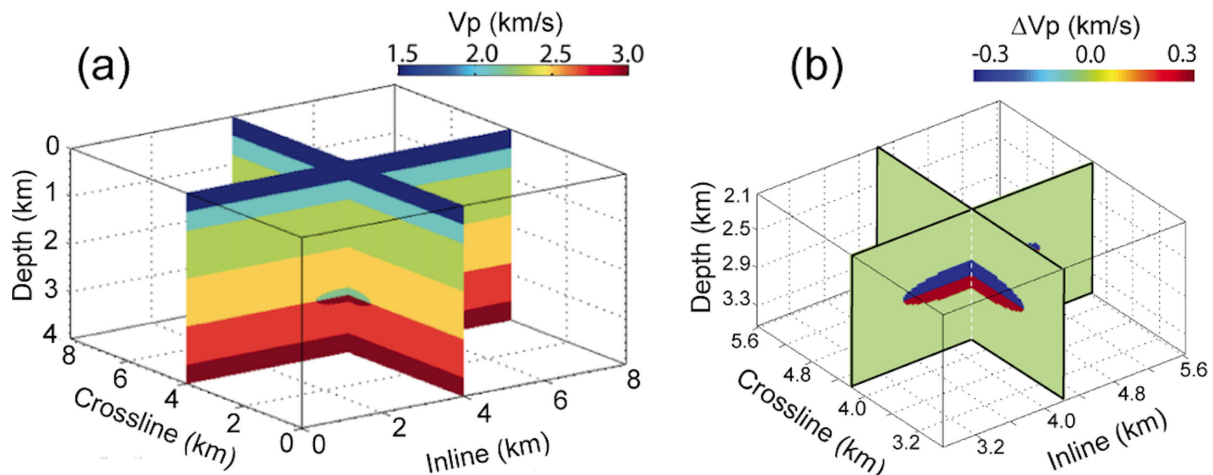


**Figure 4.** Initial 3-D volume of  $P$ -wave velocity (a) and zoom on the model perturbation (b).

the model with 20 m cubic cells, representing a uniform mesh of  $400 \times 200 \times 400$  grid points with total number of  $32 \times 10^6$  nodes. The central part of the model contains a 3-D ellipsoidal perturbation extending by  $1.4 \times 0.6 \times 1.4$  km in  $x, z$  (Fig. 4b). The velocity perturbation is placed at 2.8 km depth and consists of two lens bodies with  $P$ - and  $S$ -wave anomalies of  $\pm 0.3 \text{ km s}^{-1}$  and  $\pm 0.15 \text{ km s}^{-1}$ , respectively. C-PMLs were used at all boundaries of 10-grid point length. We use a Ricker wavelet with 7 Hz dominant

frequency as a source, placed in water layer at 10 m depth and at horizontal coordinates of (1.0, 4.0) km in  $x, y$  directions.

Fig. 5 shows the recalculated wavefield along a vertical slice going through the middle of the crossline direction on initial and modified models, which correspond to the models before and after removal of the lens-shaped anomaly, respectively. The initial  $V_p$  model is presented in Fig. 5(a). Fig. 5(b) demonstrates a snapshot of the wavefield (normal component of stress,  $\tau_{xx}$ ), which was

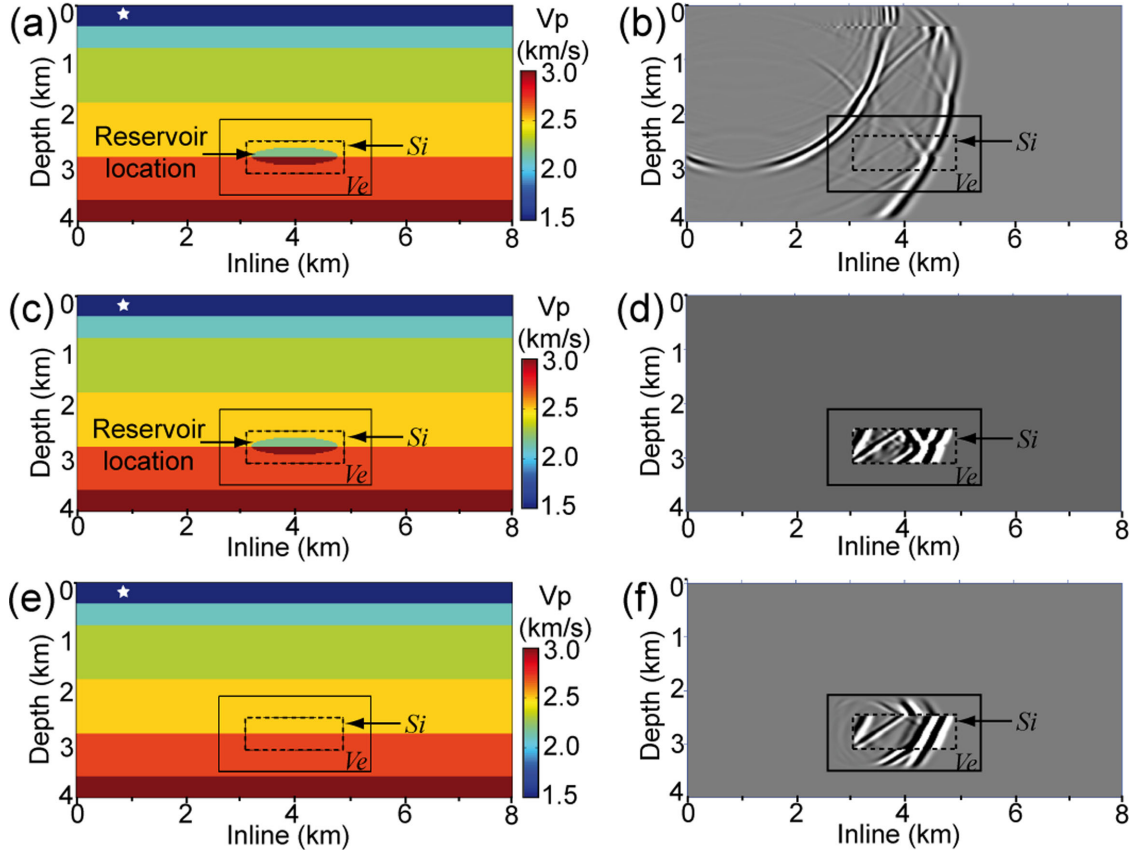


**Figure 5.** Wavefield recalculation using FD-injection method. (a, c, e) Vertical slices of  $P$ -wave velocity through the middle of the model. (b, d, f) Corresponding snapshots of normal stress at 2.1 s. (b) The snapshot was calculated on the whole initial model. Both remaining snapshots were calculated within the subvolume  $V_e$  using the wavefield injection across the surface  $S_i$ : on the initial model (d) and on the model after removal of the lens-shaped anomaly (f). White star indicates a shot position.

obtained after 2.1 s of the source insertion from the full FD-simulation on this initial model. As it was described previously, during the full modelling at each time step the wavefield from three grid points around the injection surface  $S_i$  is stored in an external file. By injecting this wavefield using eqs (9a) and (9b), the response inside the submesh  $V_e$  can be calculated on the initial and modified models. If the injection volume contains the initial model (Fig. 5c), then the wavefield inside  $V_e \cap \bar{V}_i$  would be equal to zero (Fig. 5d). While for the case of model with the removed anomaly (Fig. 5e), the wavefield inside  $V_e \cap \bar{V}_i$  corresponds to the difference between the wavefields from the initial and modified models (Fig. 5f). To obtain updated seismograms on the surface, the residual wavefield from some recording array  $S'_e$  should be extrapolated to the surface receiver positions using the Green's function and subsequently added to the initial response (eq. 9c).

In this example, by restricting the FD-simulation to the small subvolume  $V_e$ , the wavefield was re-computed about 25 times faster than the modelling inside the whole 3-D volume. Therefore, the FDIM can produce synthetic data sets for a localized waveform inversion in a very efficient manner. Another potential benefit of FD-injection for time-lapse inversion is that little energy will be incident on absorbing boundary of the truncated model (most of it is attenuated by the injection surface). The width of the absorbing boundaries can therefore be made a lot smaller (J.O. Robertsson, personal communication, 2014).

The next section briefly covers the main theoretical and computational aspects of 3-D elastic waveform inversion.

#### 4 3-D ELASTIC FULL WAVEFORM INVERSION

The goal of elastic FWI is to obtain a detailed seismic structure by fitting synthetic data to observed data. The inversion scheme implemented in this study is based on the theoretical frameworks of Tarantola (1984) and Mora (1987). In this section we recall the methodology briefly but more details on 3-D elastic FWI can be found in Borisov & Singh (2015).

The algorithm is driven by an iterative minimization of the difference between the synthetics ( $d_{\text{syn}}(\mathbf{m})$ ) for model  $\mathbf{m}$  and the observed data ( $d_{\text{obs}}$ ) in the least-squares sense ( $l_2$ -norm) for all shots:

$$S(\mathbf{m}) = \sum_{\text{shots}} \int_0^T dt \sum_{\text{recs}} [d_{\text{syn}}(\mathbf{m}) - d_{\text{obs}}]^2 = [\mathbf{d}_{\text{syn}} - \mathbf{d}_{\text{obs}}]^T [\mathbf{d}_{\text{syn}} - \mathbf{d}_{\text{obs}}], \quad (10)$$

where  $S$  is a misfit function,  $t$  is a time step and  $T$  is a total recording time and  $\mathbf{d}$  is discretized vector for all the shots and all the time increments of data  $d$ .

Local minimization of  $S$  in the vicinity of  $\mathbf{m}$  ends up with a set of normal equations:

$$(J^T J)^{-1} \delta \mathbf{m} = -\frac{\partial}{\partial \mathbf{m}} S(\mathbf{m}) \quad (11)$$

with Jacobian Matrix  $J$ :

$$J = \frac{\partial}{\partial \mathbf{m}} \mathbf{d}_{\text{syn}}(\mathbf{m}) \quad (12)$$

and the right-hand side is the gradient direction ( $g$ ):

$$g = \frac{\partial}{\partial \mathbf{m}} S(\mathbf{m}) = J^T (\mathbf{d}_{\text{syn}}(\mathbf{m}) - \mathbf{d}_{\text{obs}}) \sum_{\text{shots}} \int_0^T dt \left( \vec{u} \cdot \vec{\psi} \right) \quad (13)$$

which can be expressed as a cross-correlation of the forward modelled wavefield,  $\vec{u}$  and the back-propagated residuals  $\vec{\psi}$ . In our inversion we assume the Hessian matrix  $J^T J$  as an identity matrix and use conjugate gradient methods using  $g$  direction for each iteration.

Eq. (13) allows us to determine the gradient for the Lamé parameters ( $\delta\hat{\lambda}$ ,  $\delta\hat{\mu}$ ) in terms of the stress components:

$$\begin{aligned} \delta\hat{\lambda} &= -\frac{1}{9(3\lambda + 2\mu)^2} \sum_{\text{shots}} \int_0^T dt \left( \vec{\tau}_{xx} + \vec{\tau}_{yy} + \vec{\tau}_{zz} \right) \left( \vec{\tau}_{xx} + \vec{\tau}_{yy} + \vec{\tau}_{zz} \right), \\ \delta\hat{\mu} &= -\frac{4(\lambda + \mu)^2 + 2\lambda^2}{2\mu^2(3\lambda + 2\mu)^2} \sum_{\text{shots}} \int_0^T dt \left( \vec{\tau}_{xx}\vec{\tau}_{xx} + \vec{\tau}_{yy}\vec{\tau}_{yy} + \vec{\tau}_{zz}\vec{\tau}_{zz} \right) \\ &\quad - \frac{\lambda^2 - 4\lambda(\lambda + \mu)}{4\mu^2(3\lambda + 2\mu)^2} \sum_{\text{shots}} \int_0^T dt \left( \vec{\tau}_{xx}\vec{\tau}_{yy} + \vec{\tau}_{xx}\vec{\tau}_{zz} + \vec{\tau}_{yy}\vec{\tau}_{zz} \right) \\ &\quad + \vec{\tau}_{yy}\vec{\tau}_{xx} + \vec{\tau}_{zz}\vec{\tau}_{xx} + \vec{\tau}_{zz}\vec{\tau}_{yy} \\ &\quad - \frac{1}{\mu^2} \sum_{\text{shots}} \int_0^T dt \left( \vec{\tau}_{xz}\vec{\tau}_{xz} + \vec{\tau}_{xy}\vec{\tau}_{xy} + \vec{\tau}_{yz}\vec{\tau}_{yz} \right). \end{aligned} \quad (14)$$

As Lamé parameters are poorly resolved (e.g. Tarantola 1986), these values are converted to the gradient for  $P$ - and  $S$ -wave velocities ( $\delta\hat{V}_p$ ,  $\delta\hat{V}_s$ ) using following equations (Mora 1987):

$$\begin{aligned} \delta\hat{V}_p &= 2\rho V_p \delta\hat{\lambda}, \\ \delta\hat{V}_s &= -4\rho V_s \delta\hat{\lambda} + 2\rho V_s \delta\hat{\mu}. \end{aligned} \quad (15)$$

The density parameter being difficult to resolve is not inverted and simply updated by linking to the  $V_p$  using Gardner *et al.* (1974) and Hamilton (1978) relationships, depending on the depth. At the end of each iteration ( $n$ ), the model  $m$  is updated using the following expression

$$m_{n+1} = m_n - \eta_n c_n, \quad (16)$$

where  $c$  is a conditioned gradient direction and  $\eta$  is an optimal step length at iteration  $n$ , calculated with a linear assumption (Pica *et al.* 1990):

$$\eta_n = \varepsilon \frac{(\mathbf{d}_{\text{pert}} - \mathbf{d}_{\text{syn}})^T (\mathbf{d}_{\text{syn}} - \mathbf{d}_{\text{obs}})}{(\mathbf{d}_{\text{pert}} - \mathbf{d}_{\text{syn}})^T (\mathbf{d}_{\text{pert}} - \mathbf{d}_{\text{syn}})}. \quad (17)$$

In eq. (17), the term  $\mathbf{d}_{\text{pert}}$  represent synthetics generated by a small known model perturbation  $\varepsilon$ , which is generally assumed to be less than one per cent of maximal  $P$ -wave velocity. Eq. (17) constrains the inversion to remain in the vicinity of the current model and requires a linear approximation. We have implemented inversion in the time domain and the algorithm enables the simultaneous inversion of both  $P$ - and  $S$ - wave velocities. As compared to the frequency domain approach (Virieux *et al.* 2012), it provides straightforward and efficient implementation using parallel computing facilities, and affordable memory requirements for 3-D elastic FWI (Borisov & Singh 2015).

#### 4.1 Example of 3-D elastic inversion in the full volume

Before we perform the localized inversion for time-lapse mode, we demonstrate an example of elastic waveform inversion in time-lapse mode for a full 3-D isotropic model, shown in Fig. 4. In this

experiment, a lens-body perturbation is included in the baseline model, which was completely removed in the time-lapse model. In our approach, we assume that the velocity model from the baseline survey is previously established by means of FWI and is perfectly known. The baseline model is considered as a starting model for the inversion in order to retrieve the local time-lapse perturbation. The seismic data were generated using a point source, represented by a Ricker wavelet with a dominant frequency of 7 Hz. In order to reduce the computational time, the minimum  $S$ -wave velocity was specifically chosen to be high (about 1.3 km s<sup>-1</sup>). ‘Low’ seafloor with  $S$ -wave velocities less than 1.0 km s<sup>-1</sup> is more frequently encountered in the typical lithologies than the ‘high’ velocity (e.g. Sheriff & Geldart 1995; Sears 2007). However, the  $S$ -wave velocity allowed us to reduce the computational time significantly by using a bigger space and time discretization. For the geological configurations with low  $S$ -wave velocities, where the amplitude of mode-converted waves at sea bottom is small, an efficient hierarchical strategy can be implemented to improve the  $V_s$  results in the manner of Sears *et al.* (2010). In order to model the elastic wavefield accurately in this example, the space and time discretization were chosen to be 20 m and 3 ms, respectively. Each source is placed in water layer at a depth of 10 m, which is a realistic value for a standard marine survey. The overall computational time in our implementation linearly increases with the number of sources. Therefore, to accelerate the delivery of inversion results only forty-nine sources were used, providing a sparse mesh of 7 × 7 shots, placed in a horizontal plane 1 km apart. 8281 (91 × 91) ocean bottom cable receivers regularly spaced at 80 m interval were placed at the seafloor at 200 m depth. Each receiver measured three velocity components. C-PML was implemented at all boundaries with 10-grid point length. This allowed for efficient wavefield absorption from all boundaries of the model. Therefore, a free surface was not implemented in this synthetic study, and thus the surface multiples were not taken into account.

The results of 3-D elastic inversion using 1024 processor cores are shown in Figs 6–8. Fig. 6 illustrates 4-D model perturbations for  $P$ -wave (panel a) and  $S$ -wave velocities (panel b) retrieved after 30 FWI iterations. After comparison with the true perturbation (Fig. 4b), the shape of the anomaly could be easily recognized. Fig. 7 illustrates three vertical slices going through the middle of crossline direction of the model shown in Fig. 6, for both  $P$ -wave (panel a) and  $S$ -wave velocities (panel b). One can note that the result for the shear wave velocity has a better resolution, which is explained by the shorter wavelength of  $S$  wave. In Fig. 8, the velocity profiles for  $P$ - and  $S$ -wave velocities (panels a and b, respectively) going through the middle of the inline direction further demonstrate a good agreement between the true and recovered perturbations. The data (vertical velocity component,  $v_z$ ) from one shot located in the middle of the model are shown in Fig. 9. There is a significant reduction of the residual amplitude after 30 inversion iterations in comparison with the initial residuals (Figs 9e and d, respectively). The final values of the normalized FWI misfit are less than 20 per cent (Fig. 14).

We suppose that the quality of the FWI results could be further improved if a more dense sources and receivers coverage was used in the experiment. Additional 10–20 iterations could be beneficial for the quality of the inversion results as well, but due to the limitations in the available computer resources we could not afford to further iterate the inversion. In general, for a given experimental setup and for the available frequency range, our 3-D elastic FWI code applied in the full volume provides adequate velocity updates and retrieves the 4-D anomaly well enough. Successfulness of the inversion in this example is explained by the combination of several

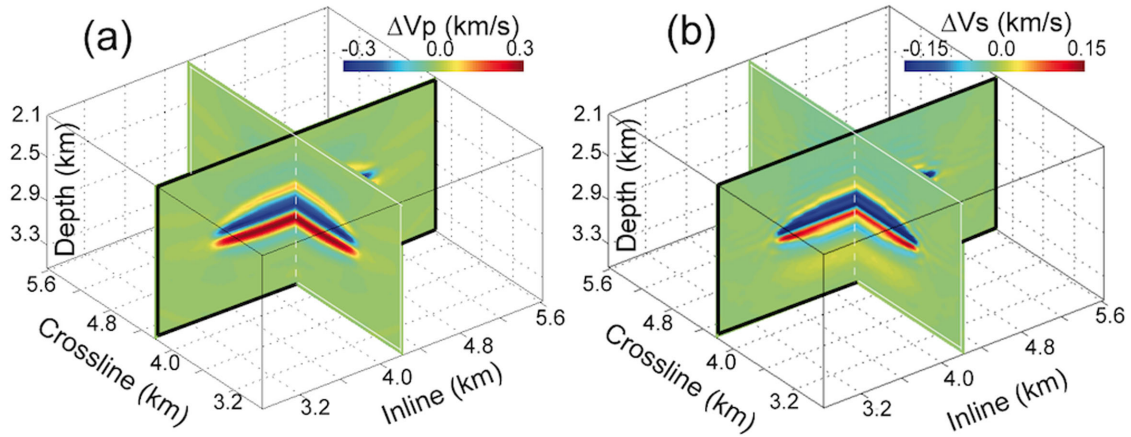


**Figure 6.** 3-D view of inverted  $P$ -wave (a) and  $S$ -wave (b) velocity perturbations after applying FWI in the full domain.

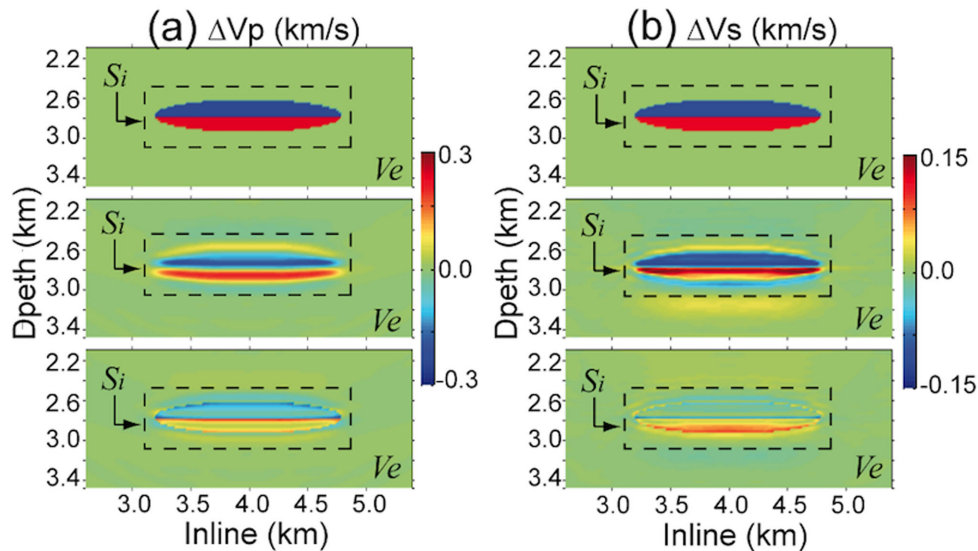


**Figure 7.** Vertical slices of inverted  $P$ -wave (a) and  $S$ -wave (b) velocity perturbations in the case of full domain FWI. The slices spread through the middle of the crossline direction shown in Fig. 6 and highlighted by the thick black boundary. The corresponding slices are the true (top), recovered (middle) and the residual (bottom) velocity perturbation.

favourable factors, which strongly benefit synthetic FWI: perfectly known source wavelet, absence of noise, very accurate estimate of the starting model. In reality, these factors will definitely play a crucial role and make the FWI application much more challenging. In this synthetic study, we do not tackle these well-known obstacles. We are rather interested in comparison of the inversion results performed in the full domain with the localized FWI approach, presented in the next section.

#### 4.2 Example of localized 3-D elastic inversion

Here we present an example of efficient reservoir monitoring with the aid of localized time lapse FWI. The example demonstrates the application of the localized FWI on the model used for full volume inversion.

We started by integration of the localized forward modelling scheme within the 3-D elastic FWI algorithm. To simplify the experiment, we initially placed all receivers at some datum close to the zone of interest (Fig. 2, surface  $S'_e$ ). This was done in order to calculate directly the difference between observed and modelled data inside the subvolume  $V_e$ , thus avoiding the extrapolation step.

As it was previously described, the data observed on the surface can be propagated to a new depth assuming that the velocity model is well constrained for a baseline survey using eq. (9c). The re-datuming of the observed data will not significantly increase the total computational time as it should be done only once before the first inversion iteration. The corresponding geometry with seismic receivers at depth can also represent a real situation, for example, a deep horizontal well or a vertical seismic profile survey.

As in the case of the full domain FWI experiment, there are 49 sources represented by the Ricker wavelet with the dominant frequency of 7 Hz and sparse spacing of 1 km. Due to the reduced number of receivers in the subvolume, we use smaller grid spacing here in this case: the distance between receivers is 40 m in both horizontal and vertical directions. This time only  $56 \times 56$  geophones were used, providing smaller receiver coverage of  $2.2 \times 2.2$  km. The reduced maximum offset will occur when we extrapolate the wavefield close to the target reflector. The extrapolation will also increase moveout, increasing the sensitivity of the waveform inversion. Indeed, one can notice that higher wavenumbers are retrieved in the localized approach (Fig. 12) due to the reduced offset in comparison with the full-volume experiment (Fig. 8).

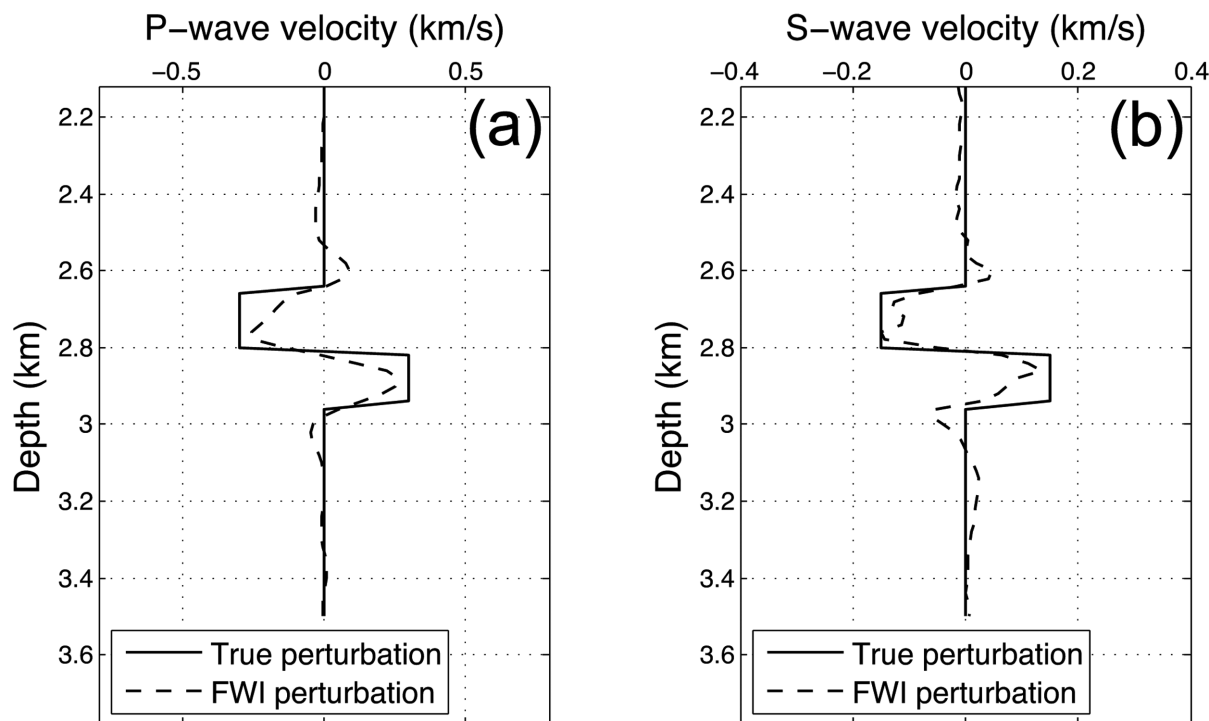


**Figure 8.** Vertical profiles of inverted  $P$ -wave (a) and  $S$ -wave (b) velocity perturbations obtained after applying FWI in the full domain. The velocity logs taken at the middle of the inline direction (at 4 km) shown in Fig. 7.

After integration of the FDIM within the FWI, the inversion results were achieved on a regular desktop computer with only eight processor cores. The obtained results equally demonstrate a good recovery of main features for both  $P$ - and  $S$ -wave velocities (Figs 10–12). The zoom on the 3-D anomaly is shown in Fig. 10, where the lens shape of the anomaly could be easily recognized. Fig. 11 demonstrates three vertical slices that pass through the middle of the crossline direction in the Fig. 10. In Fig. 12, the velocity profiles for  $P$ - and  $S$ -wave velocities (panels a and b, respectively) through the middle of the inline direction further demonstrate a good agreement between the true and recovered perturbations.

Fig. 13 shows vertical velocity component ( $v_z$ ) from one source located in the middle of the model. Note the reductions of the residual amplitude after 30 inversion iterations in comparison with the initial residuals (Figs 13d and c, respectively). In this example, the final values of the normalized FWI misfit are reduced by more than 95 per cent after 30 iterations (Fig. 14). Comparison of the waveform inversion results from the full domain and using the localized strategy demonstrate that our strategy allows recover accurately 4-D model perturbation in a very efficient manner. One can also note that full-volume FWI has a slower convergence and bigger final values of the misfit. This is due to the fact that the conventional FWI inverts for a very large number of the parameters in the entire volume, and the gradient direction for such a large number of parameters will be more complicated than those for localized FWI where the number of model parameters is much smaller. Second, the moveout for the localized inversion is much larger than that for the full volume inversion, making the local inversion more robust.

### 4.3 Computational efficiency

Most of the work presented here was performed on a CURIE supercomputer. We used the computer nodes that were specifically

targeted for MPI parallel codes. Each node consisted in 2 eight-core Intel processors Sandy Bridge EP (E5-2680) 2.7 GHz, 64 GB of RAM (Random Access Memory), and 1 local SSD (Solid-State Drive) disks as a data storage. The use of SSD discs in our implementation provided significant improvements in the efficiency, because they allow the acceleration of an inter-node communication due to faster input/output operations. This was particularly important when a large number of processors were used. A typical submitted job for the 3-D elastic waveform inversion utilized simultaneously 64 nodes or 1024 cores, and took about 1 day of continuous calculation. Table 1 shows the comparison of some computational parameters for two cases: (1) FWI using surface geometry, which was undertaken within the whole model and (2) the localized inversion using the FDIM.

By reducing the model space, significant computational savings were obtained, which allowed to perform inversion on a regular desktop with only eight processor cores instead of using high-performance cluster. We sped up the computations by a factor of 25, while the memory requirements (RAM) were reduced by a factor of 30. Only the memory storage on a hard disk was increased from 300 GB to 600 GB in order to keep the data used for wavefield injection. However, this does not represent a critical issue, because currently the disk space of such volume is quite cheap and affordable. Potentially, the total computational time within localized inversion could be further reduced, if only a part of the total recording time was considered. Indeed, significant amount of time is generally required for the wavefield to propagate from the sources located on the surface to the target, and then back to the surface receivers. In the localized approach the receivers are placed close to the zone of interest, therefore, some part of the total recording time (i.e. at the beginning and in the end of the wavefield propagation) could potentially not be taken into account.

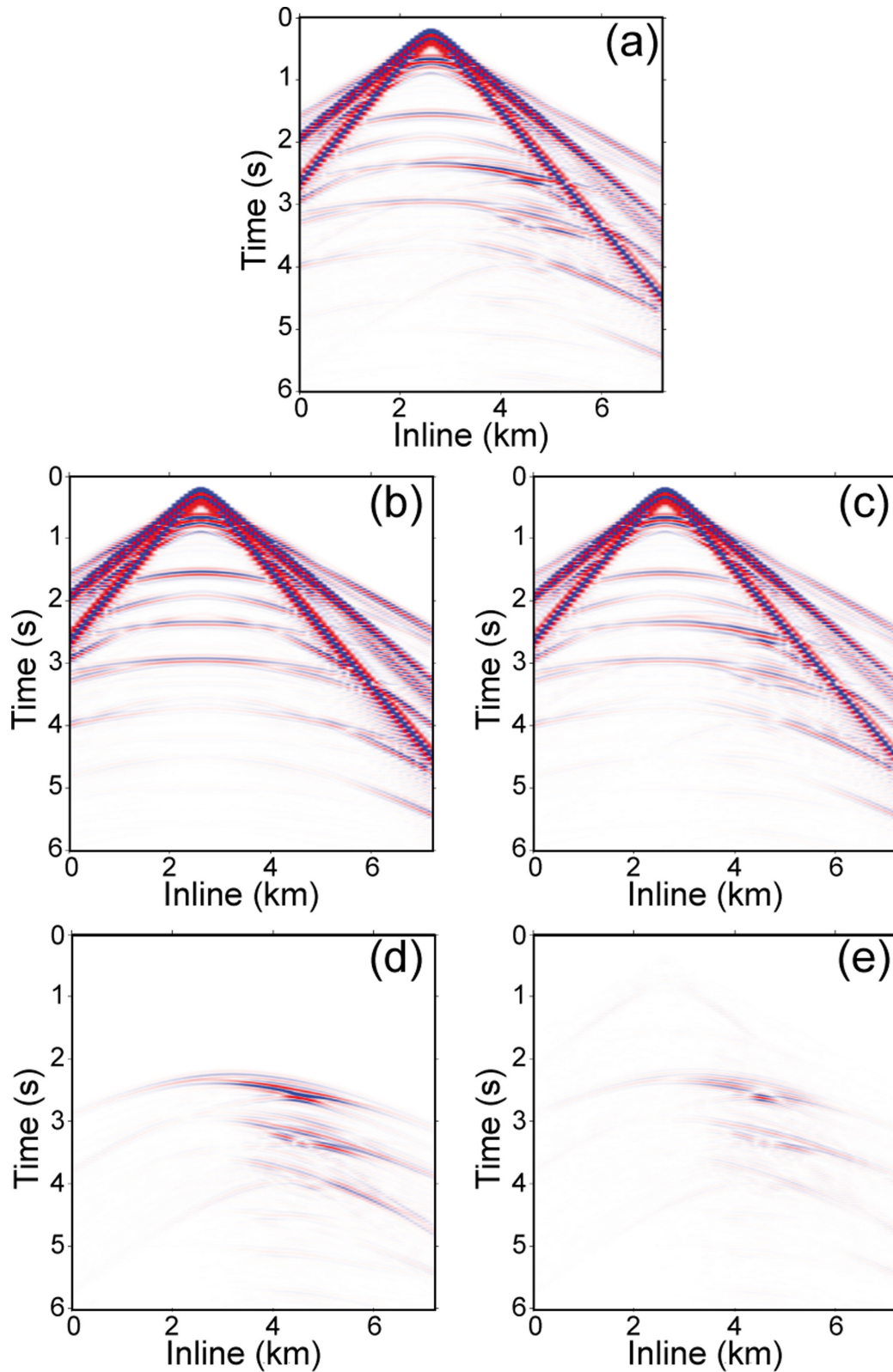


**Figure 9.** Vertical velocity component ( $v_z$ ) from one source located in the middle of the model. Five panels are shown: (a) observed, (b) initial synthetics, (c) final synthetics, (d) initial residuals and (e) final residuals. Note the reductions of the residual amplitude (e) after 30 inversion iterations in comparison with the initial one (d).

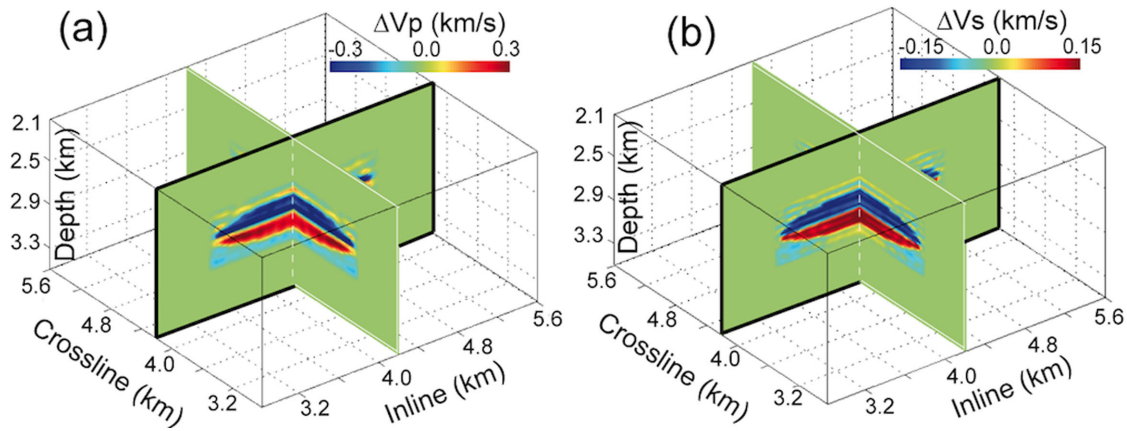


Figure 10. 3-D view of inverted  $P$ -wave (a) and  $S$ -wave (b) velocity perturbations after applying localized FWI.

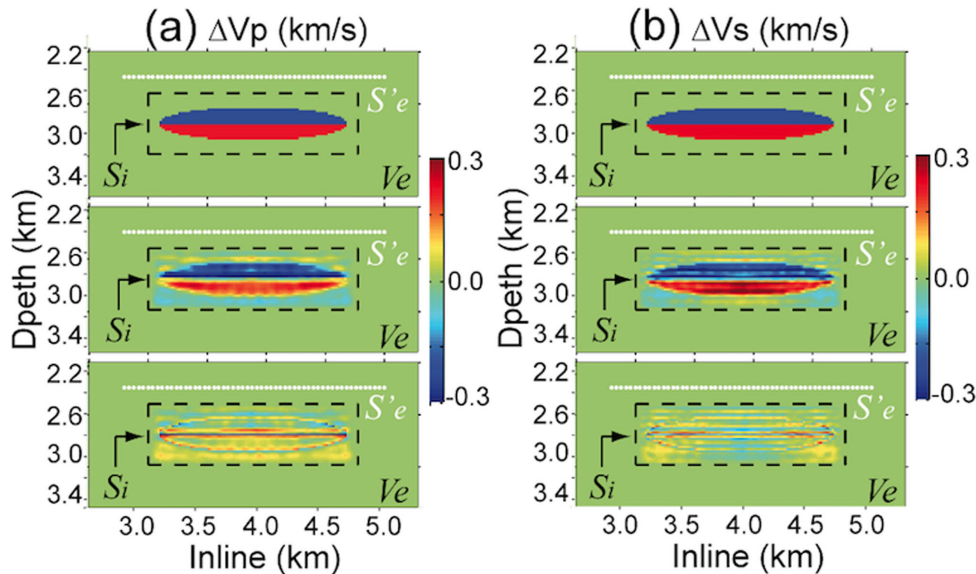


Figure 11. Vertical slices of inverted  $P$ -wave (a) and  $S$ -wave (b) velocity perturbations in the case of localized FWI. The slices spread through the middle of the crossline direction shown in Fig. 10 and highlighted by thick black boundary. The corresponding slices are the true (top), recovered (middle) and the residual (bottom) velocity perturbation.

## 5 DISCUSSIONS AND CONCLUSIONS

We have developed a 3-D elastic FWI scheme using an FDIM and successfully applied it to synthetic time-lapse data, demonstrating the feasibility of our algorithm. We have also compared the results from the conventional FWI, performed on the whole model and FDIM based FWI using synthetic time-lapse experiment. The velocity models obtained from the localized strategy have shown no degradation in the final results. Moreover, the computational time was reduced by a factor of 25, and memory requirements (RAM) were reduced by a factor of 30. This significant decrease in computation time allowed us to perform all calculations on a regular desktop with only eight processor cores instead of using computer cluster with a large number of processors. The obtained dramatic computational savings show a big potential for time-lapse monitoring for real data applications, where the seismic vintages are frequently acquired over the same area, using prohibitively expensive but more accurate and realistic 3-D elastic formulation. This makes the algorithm extremely useful for production-oriented applications with well-identified reservoir sequences for a time-lapse survey.

In this short synthetic study, we do not perform the extrapolation process and the wavefield was recorded directly at virtual receivers. The extrapolation could provide seismic records at different datum with sufficient level of accuracy, assuming the background velocity model used for calculation of Green's functions is well constrained between the surface and virtual receivers. We expect that the quality of the extrapolated data should be well reproduced at all offsets for our geometry, if an adequate receivers sampling is chosen. This is because the regions with most important contribution for the calculation of the extrapolated wavefield, which we can call as 'phase stationary regions' (Snieder *et al.* 2006), are concentrated essentially in the vicinity of ray paths, which are covered in this experiment. Therefore, we do not expect any significant degradation at the model edges in this geometry. We also suggest that the resulting errors should lie within the domain of applicability of the waveform inversion. However, future work should be carried out to explore the influence of some aspects as the errors in overburden, 4-D repeatability and noise on the inverted parameters.

It is worth noting that in practice the storage requirements of the injection wavefield would be a hindrance because the memory requirement is proportionally related to the size of zone of interest and

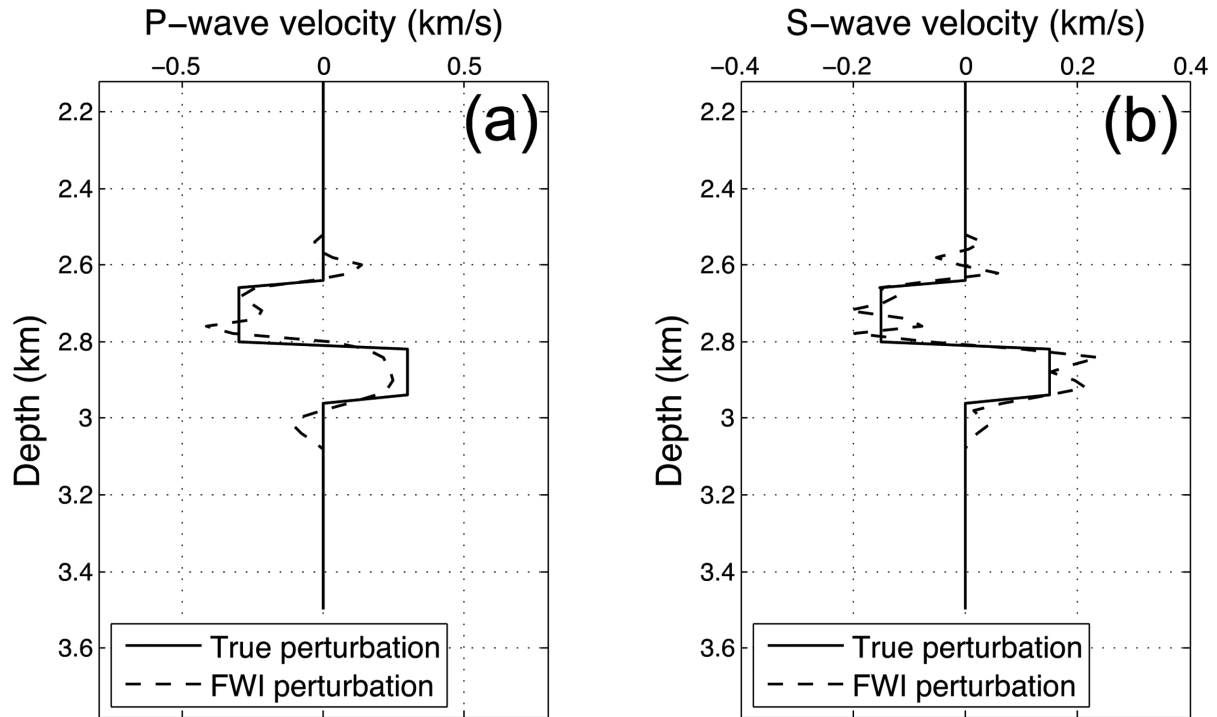


**Figure 12.** Vertical profiles of inverted  $P$ -wave (a) and  $S$ -wave (b) velocity perturbations obtained after applying localized FWI. The velocity logs taken at the middle of the inline direction (at 4 km) shown in Fig. 11.

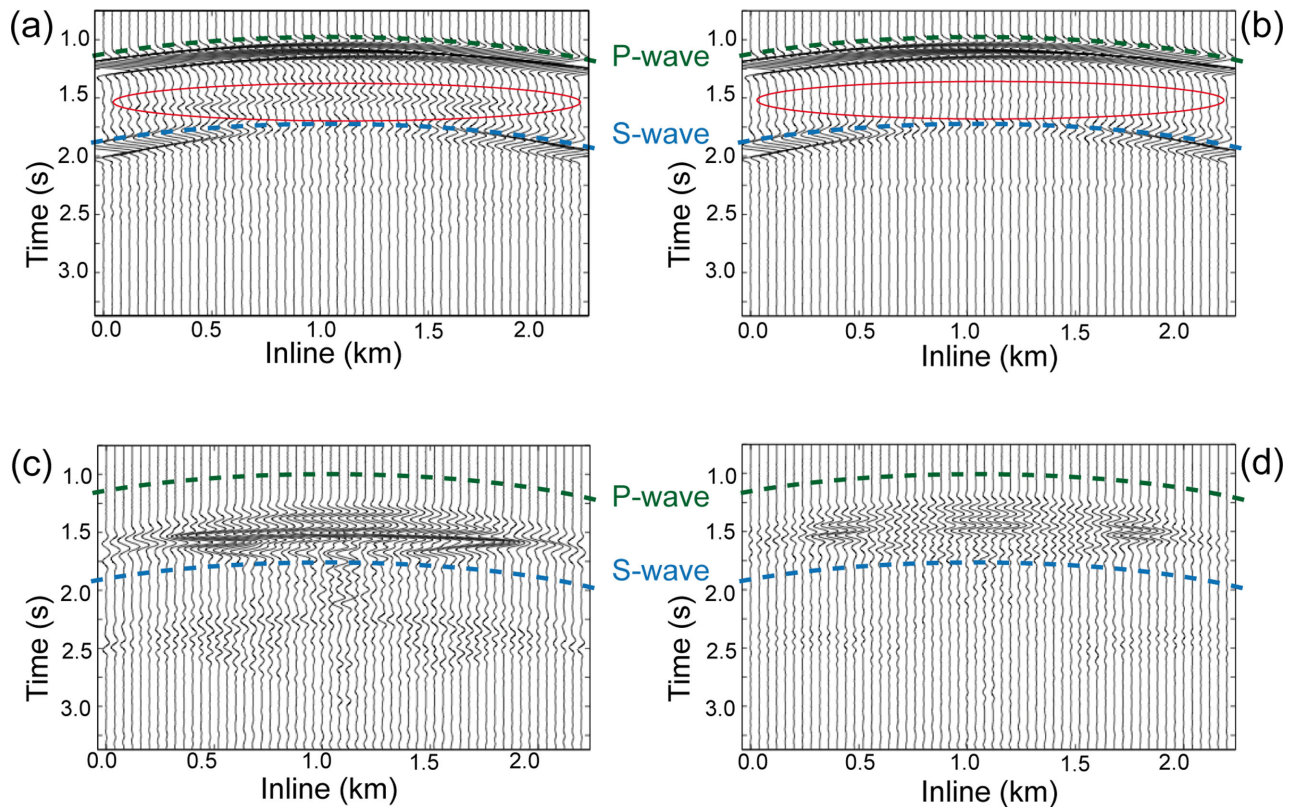


**Figure 13.** Vertical velocity component ( $v_z$ ) recorded at receiver's position in localized FWI: (a) before perturbations; (b) after perturbations; (c) the difference between (a) & (b); (d) after final FWI residuals after 30 iterations; (c) & (d) are shown on the scale increased five times in comparison with (a) & (b).

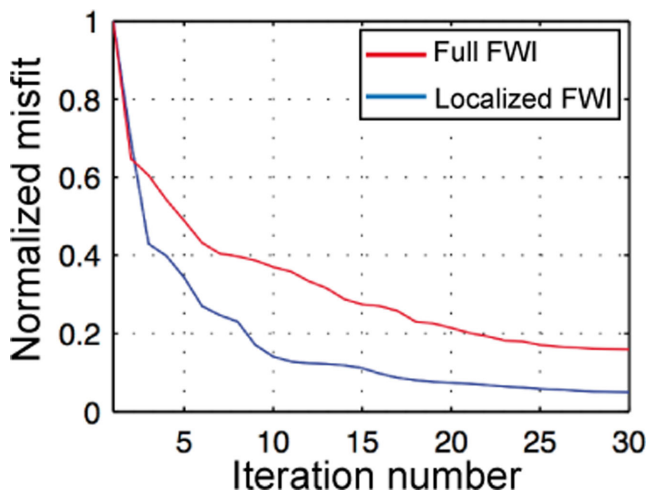


**Figure 14.** Comparison of misfit reduction for the FWI on the whole model with a surface survey (red line) and localized FWI (blue line).

**Table 1.** Comparison of the computation parameters between FWI on the whole model with a surface survey and localized FWI.

Formulation	Conventional FWI (1)	Localized FWI (2)	(1) / (2)
CPU time (h)	≈22 000	≈900	≈25 (speedup)
RAM (Gb)	≈1012	≈33	≈30
Memory storage (Gb)	≈300	≈600	≈0.5

to the number of seismic sources used in the survey. Therefore, the localized approach could be especially attractive in cases when the zone containing the model perturbations is much smaller than the full seismic survey area. Potential benefit of FDIM for time-lapse inversion is that little energy will be incident on absorbing boundary of the truncated model (most of it is attenuated by the injection surface). The width of the absorbing boundaries can therefore be made a lot smaller. The further extension could include incorporation of more physics, that is attenuation or anisotropy, or more computationally intensive optimization techniques as Gauss–Newton and Newton methods. Another aspect, which can be explored, is increasing of the resolution far beyond the frequency range provided by the traditional waveform inversion. Currently, the results of the waveform inversion are limited to the low frequencies and incorporation of higher frequency can increase the computational expenses dramatically. Therefore, the accelerations provided by the localized inversion strategy can help with enlarging the bandwidth of the inverted data. For example, one can use a low-frequency inversion for the base model using the whole data and use high-frequency inversion in the localized area using our FDIM, increasing the resolution significantly.

## ACKNOWLEDGEMENTS

We thank LITHOS consortium for founding this project. We are also very grateful to Gillian Royle from CGG for 2-D prototype of FDIM and fruitful discussions. We thank the editors J. Virieux and Yder Masson and an anonymous reviewer for comments and suggestions that improved the paper. We also thank Johan Robertsson, Stéphane Operto, François Audebert and James Martin for very useful dis-

cussions. This work was granted access to the HPC resources of TGCC under the allocation t2013047092 made by GENCI (Grand Équipement National de Calcul Intensif). A significant part of the calculations in this work was performed on the local cluster at the Paris Institute of Earth Science (IPGP).

## REFERENCES

- Aki, K. & Richards, P.G., 2002. *Quantitative Seismology*, Vol. 1, University Science Books.
- Alterman, Z. & Karal, F., 1968. Propagation of elastic waves in layered media by finite difference methods, *Bull. seism. Soc. Am.*, **58**(1), 367–398.
- Arnulf, A., Harding, A., Singh, S., Kent, G. & Crawford, W., 2012. Fine-scale velocity structure of upper oceanic crust from full waveform inversion of downward continued seismic reflection data at the lucky strike volcano, mid-atlantic ridge, *Geophys. Res. Lett.*, **39**(8), doi:10.1029/2012gl051064.
- Asnaashari, A., Brossier, R., Garambois, S., Audebert, F., Thore, P. & Virieux, J., 2011. Sensitivity analysis of time-lapse images obtained by differential waveform inversion with respect to reference model, in *2011 SEG Annual Meeting*, Society of Exploration Geophysicists, doi:10.1190/1.3627707.
- Asnaashari, A., Brossier, R., Garambois, S., Audebert, F., Thore, P. & Virieux, J., 2013. Regularized seismic full waveform inversion with prior model information, *Geophysics*, **78**(2), R25–R36.
- Asnaashari, A., Brossier, R., Garambois, S., Audebert, F., Thore, P. & Virieux, J., 2015. Time-lapse seismic imaging using regularized full-waveform inversion with a prior model: which strategy?, *Geophys. Prospect.*, **63**(1), 78–98.
- Barnes, C. & Charara, M., 2009. The domain of applicability of acoustic full-waveform inversion for marine seismic data, *Geophysics*, **74**(6), WCC91–WCC103.
- Ben-Hadj-Ali, H., Operto, S. & Virieux, J., 2008. Velocity model building by 3d frequency-domain, full-waveform inversion of wide-aperture seismic data, *Geophysics*, **73**(5), VE101–VE117.
- Boore, D.M., 1972. Finite difference methods for seismic wave propagation in heterogeneous materials, in *Methods in Computational Physics*, Vol. 11, pp. 1–37, ed. Bolt, B.A., Academic Press.
- Borisov, D. & Satish, S., 2013. Elastic 3D full waveform inversion in the time domain, in *75th EAGE Conference & Exhibition Incorporating SPE EUROPEC 2013*, doi:10.3997/2214-4609.20130293.
- Borisov, D. & Singh, S.C., 2015. Three-dimensional elastic full waveform inversion in marine environment using multi-component ocean-bottom cables: synthetic study, *Geophys. J. Int.*, **201**(3), 1215–1234.
- Bouchon, M. & Sánchez-Sesma, F.J., 2007. Boundary integral equations and boundary elements methods in elastodynamics, *Advances in Geophysics*, **48**, 157–189.
- Brossier, R., Operto, S. & Virieux, J., 2009. Seismic imaging of complex onshore structures by 2D elastic frequency-domain full-waveform inversion, *Geophysics*, **74**(6), WCC105–WCC118.
- Butzer, S., Kurzmann, A. & Bohlen, T., 2013. 3D elastic full-waveform inversion of small-scale heterogeneities in transmission geometry, *Geophys. Prospect.*, **61**(6), 1238–1251.
- Capdeville, Y., Larmat, C., Vilotte, J., Montagner, J. & de Sismologie, D., 2002. Numerical simulation of the scattering induced by a localized plume-like anomaly using a coupled spectral element and modal solution method, *Geophys. Res. Lett.*, **29**(9), doi:10.1029/2001GL013747.
- Capdeville, Y., Chaljub, E. & Montagner, J., 2003. Coupling the spectral element method with a modal solution for elastic wave propagation in global earth models, *Geophys. J. Int.*, **152**(1), 34–67.
- Dong, S., 2008. Fast three-dimensional target-oriented reverse time datuming, *PhD thesis*, The University of Utah.
- Dong, S., Luo, Y., Xiao, X., Chávez-Pérez, S. & Schuster, G.T., 2009. Fast 3D target-oriented reverse-time datuming, *Geophysics*, **74**(6), WCA141–WCA151.

- Fichtner, A., Kennett, B.L., Igel, H. & Bunge, H.-P., 2009. Full seismic waveform tomography for upper-mantle structure in the australasian region using adjoint methods, *Geophys. J. Int.*, **179**(3), 1703–1725.
- French, S., Lekic, V. & Romanowicz, B., 2013. Waveform tomography reveals channeled flow at the base of the oceanic asthenosphere, *Science*, **342**(6155), 227–230.
- Gardner, G., Gardner, L. & Gregory, A., 1974. Formation velocity and density—the diagnostic basics for stratigraphic traps, *Geophysics*, **39**(6), 770–780.
- Godinho, L., Mendes, P.A., Tadeu, A., Cadena-Isaza, A., Smerzini, C., Sánchez-Sesma, F., Madec, R. & Komatitsch, D., 2009. Numerical simulation of ground rotations along 2D topographical profiles under the incidence of elastic plane waves, *Bull. seism. Soc. Am.*, **99**(2B), 1147–1161.
- Gosselet, A. & Singh, S., 2007. CO<sub>2</sub> thin beds imaging using full waveform inversion—applications to synthetic and real time—lapse data, in *69th EAGE Conference & Exhibition*, doi:10.3997/2214-4609.201401593.
- Graves, R.W., 1996. Simulating seismic wave propagation in 3d elastic media using staggered-grid finite differences, *Bull. seism. Soc. Am.*, **86**(4), 1091–1106.
- Guasch, L., Warner, M., Nangoo, T., Morgan, J., Umpleby, A., Štekl, I. & Shah, N., 2012. Elastic 3D full-waveform inversion, in *82nd Annual International Meeting*, SEG, Expanded Abstracts, SI6, 8.
- Halliday, D. & Curtis, A., 2010. An interferometric theory of source-receiver scattering and imaging, *Geophysics*, **75**(6), SA95–SA103.
- Hamilton, E.L., 1978. Sound velocity–density relations in sea-floor sediments and rocks, *J. acoust. Soc. Am.*, **63**(2), 366–377.
- Hicks, G.J., 2002. Arbitrary source and receiver positioning in finite-difference schemes using kaiser windowed sinc functions, *Geophysics*, **67**(1), 156–165.
- Kawai, K., Konishi, K., Geller, R.J. & Fuji, N., 2014. Methods for inversion of body-wave waveforms for localized three-dimensional seismic structure and an application to D' structure beneath Central America, *Geophys. J. Int.*, **197**(1), 495–524.
- Komatitsch, D. & Martin, R., 2007. An unsplit convolutional perfectly matched layer improved at grazing incidence for the seismic wave equation, *Geophysics*, **72**(5), SM155–SM167.
- Konishi, K., Kawai, K., Geller, R.J. & Fuji, N., 2014. Waveform inversion for localized three-dimensional seismic velocity structure in the lowermost mantle beneath the Western Pacific, *Geophys. J. Int.*, **199**(2), 1245–1267.
- Lailly, P., 1983. The seismic inverse problem as a sequence of before stack migrations, in *Conference on Inverse Scattering: Theory and Application*, pp. 206–220, ed. Bednar, J., Society for Industrial and Applied Mathematics, Philadelphia, PA.
- Lekić, V. & Romanowicz, B., 2011. Inferring upper-mantle structure by full waveform tomography with the spectral element method, *Geophys. J. Int.*, **185**(2), 799–831.
- Levander, A.R., 1988. Fourth-order finite-difference P-SV seismograms, *Geophysics*, **53**(11), 1425–1436.
- Madariaga, R., 1976. Dynamics of an expanding circular fault, *Bull. seism. Soc. Am.*, **66**(3), 639–666.
- Masson, Y., Cupillard, P., Capdeville, Y. & Romanowicz, B., 2013. On the numerical implementation of time-reversal mirrors for tomographic imaging, *Geophys. J. Int.*, **196**(3), 1580–1599.
- Monteiller, V., Chevrot, S., Komatitsch, D. & Fuji, N., 2013. A hybrid method to compute short-period synthetic seismograms of teleseismic body waves in a 3-D regional model, *Geophys. J. Int.*, **192**(1), 230–247.
- Mora, P., 1987. Nonlinear two-dimensional elastic inversion of multioffset seismic data, *Geophysics*, **52**(9), 1211–1228.
- Mufti, I.R., 1989. Numerical experiments with a salt dome, *Geophysics*, **54**(8), 1042–1045.
- Operto, S., Virieux, J., Dessa, J.-X. & Pascal, G., 2006. Crustal seismic imaging from multifold ocean bottom seismometer data by frequency domain full waveform tomography: Application to the eastern nankai trough, *J. geophys. Res.*, **111**(B9), doi:10.1029/2005JB003835h.
- Opršal, I., Matyska, C. & Irikura, K., 2009. The source-box wave propagation hybrid methods: general formulation and implementation, *Geophys. J. Int.*, **176**(2), 555–564.
- Pica, A., Diet, J. & Tarantola, A., 1990. Nonlinear inversion of seismic reflection data in a laterally invariant medium, *Geophysics*, **55**(3), 284–292.
- Plessix, R.-E., 2006. A review of the adjoint-state method for computing the gradient of a functional with geophysical applications, *Geophys. J. Int.*, **167**(2), 495–503.
- Plessix, R.-E., 2009. Three-dimensional frequency-domain full-waveform inversion with an iterative solver, *Geophysics*, **74**(6), WCC149–WCC157.
- Plessix, R.-E., Milcik, P., Rynja, H., Stopin, A., Matson, K. & Abri, S., 2013. Multiparameter full-waveform inversion: marine and land examples, *Leading Edge*, **32**(9), 1030–1038.
- Pratt, R., Song, Z.-M., Williamson, P. & Warner, M., 1996. Two-dimensional velocity models from wide-angle seismic data by wavefield inversion, *Geophys. J. Int.*, **124**(2), 323–340.
- Queißer, M. & Singh, S.C., 2013. Localizing CO<sub>2</sub> at sleipnerseismic images versus p-wave velocities from waveform inversion, *Geophysics*, **78**(3), B131–B146.
- Randall, C., 1989. Absorbing boundary condition for the elastic wave equation: Velocity-stress formulation, *Geophysics*, **54**(9), 1141–1152.
- Ravaut, C., Operto, S., Improta, L., Virieux, J., Herrero, A. & Dell'Aversana, P., 2004. Multiscale imaging of complex structures from multifold wide-aperture seismic data by frequency-domain full-waveform tomography: application to a thrust belt, *Geophys. J. Int.*, **159**(3), 1032–1056.
- Roberts, M.A., Singh, S. & Hornby, B.E., 2008. Investigation into the use of 2d elastic waveform inversion from look-ahead walk-away vsp surveys, *Geophys. Prospect.*, **56**(6), 883–895.
- Robertsson, J.O. & Chapman, C.H., 2000. An efficient method for calculating finite-difference seismograms after model alterations, *Geophysics*, **65**(3), 907–918.
- Routh, P., Palacharla, G., Chikichev, I. & Lazaratos, S., 2012. Full wavefield inversion of time-lapse data for improved imaging and reservoir characterization, in *2012 SEG Annual Meeting*, Society of Exploration Geophysicists, doi:10.1190/segam2012-1043.1.
- Royle, G.T., 2010. Viscoelastic full waveform inversion for ocean-bottom cable seismic data, *PhD thesis*, Institute de Physique du globe de Paris.
- Sears, T.J., 2007. Elastic full waveform inversion of multi-component ocean-bottom false seismic data, *PhD thesis*, University of Cambridge.
- Sears, T.J., Singh, S. & Barton, P., 2008. Elastic full waveform inversion of multi-component obc seismic data, *Geophys. Prospect.*, **56**(6), 843–862.
- Sears, T.J., Barton, P.J. & Singh, S.C., 2010. Elastic full waveform inversion of multicomponent ocean-bottom cable seismic data: application to Alba Field, UK North Sea, *Geophysics*, **75**(6), R109–R119.
- Sheriff, R.E. & Geldart, L.P., 1995. *Exploration Seismology*, 1995, 2nd edn, Cambridge Univ. Press.
- Shipp, R.M. & Singh, S.C., 2002. Two-dimension full wavefield inversion of wide-aperture marine seismic streamer data, *Geophys. J. Int.*, **151**(2), 325–344.
- Singh, S. & Royle, G., 2010. Time-lapse elastic full waveform inversion using injected grid method, in *72nd EAGE Conference & Exhibition*, doi:10.3997/2214-4609.201400599.
- Sirgue, L., Barkved, O., Dellinger, J., Etgen, J., Albertin, U. & Kommedal, J., 2010. Thematic Set: Full waveform inversion: the next leap forward in imaging at Valhall, *First Break*, **28**(4), 65–70.
- Snieder, R., Wapenaar, K. & Larner, K., 2006. Spurious multiples in seismic interferometry of primaries, *Geophysics*, **71**(4), SI111–SI124.
- Taflove, A. & Hagness, S.C., 2005. *Computational Electrodynamics*, Artech House.
- Tarantola, A., 1984. Inversion of seismic reflection data in the acoustic approximation, *Geophysics*, **49**(8), 1259–1266.
- Tarantola, A., 1986. A strategy for nonlinear elastic inversion of seismic reflection data, *Geophysics*, **51**(10), 1893–1903.
- Tromp, J., Tape, C. & Liu, Q., 2005. Seismic tomography, adjoint methods, time reversal and banana-doughnut kernels, *Geophys. J. Int.*, **160**(1), 195–216.
- van Manen, D.-J., Robertsson, J.O. & Curtis, A., 2007. Exact wave field simulation for finite-volume scattering problems, *J. acoust. Soc. Am.*, **122**(4), EL115–EL121.

- Vigh, D., Jiao, K. & Watts, D., 2013. Elastic full-waveform inversion using 4c data acquisition, in *75th EAGE Conference & Exhibition Incorporating SPE EUROPEC 2013*, doi:10.3997/2214-4609.20130114.
- Vigh, D., Jiao, K., Watts, D. & Sun, D., 2014. Elastic full-waveform inversion application using multicomponent measurements of seismic data collection, *Geophysics*, **79**(2), R63–R77.
- Virieux, J., 1986. P-SV wave propagation in heterogeneous media: velocity-stress finite-difference method, *Geophysics*, **51**(4), 889–901.
- Virieux, J. & Operto, S., 2009. An overview of full-waveform inversion in exploration geophysics, *Geophysics*, **74**(6), WCC1–WCC26.
- Virieux, J. *et al.*, 2012. Modelling seismic wave propagation for geophysical imaging, in *Seismic Waves – Research and Analysis*, pp. 253–304, ed. Kanao, M., InTech.
- Wapenaar, C., Cox, H. & Berkhout, A., 1992a. Elastic redatuming of multicomponent seismic data1, *Geophys. Prospect.*, **40**(4), 465–482.
- Wapenaar, C., Verschuur, D.J. & Herrmann, P., 1992b. Amplitude preprocessing of single and multicomponent seismic data, *Geophysics*, **57**(9), 1178–1188.
- Yang, D., Zheng, Y., Fehler, M. & Malcolm, A., 2012. Target-oriented time-lapse waveform inversion using virtual survey, in *2012 SEG Annual Meeting*, Society of Exploration Geophysicists, doi: 10.1190/segam2012-1308.1.
- Zheng, Y., Barton, P. & Singh, S., 2011. Strategies for elastic full waveform inversion of time-lapse ocean bottom cable (OBC) seismic data, in *2011 SEG Annual Meeting*, Society of Exploration Geophysicists, SEG-2011-4195.